Journal of Materials Chemistry C

ROYAL SOCIETY OF CHEMISTRY

COMMUNICATION

View Article Online
View Journal | View Issue

Cite this: J. Mater. Chem. C, 2022, 10, 7822

Received 31st March 2022,
Accepted 3rd May 2022

DOI: 10.1039/d2tc01297a

rsc.li/materials-c

Highly stable photomultiplication-type organic photodetectors with single polymers containing intramolecular traps as the active layer†

Zijin Zhao,‡[a] Baiqiao Liu,‡[ab] Chunyu Xu,[a] Longtao Li,[a] Ming Liu,[a] Kaixuan Yang,[a] Sang Young Jeong,[d] Han Young Woo,[d] Guangcai Yuan,*[c] Weiwei Li*[b] and Fujun Zhang*[a]

Photomultiplication-type organic photodetectors (PM-OPDs) have attracted enormous interest owing to their high sensitivity toward weak light and, especially, due to their excellent parasitic stability when using a single polymer as the active layer. Herein, three different polymers, DCP1-3, were synthesized with different amounts of $PC_{61}BM$ pendants as intramolecular traps, and they were successfully applied to high-stability PM-OPDs. Photogenerated electrons will be trapped by suspended $PC_{61}BM$ in the polymers to induce interfacial band-bending for hole tunneling injection, and the injected holes can be efficiently transported along the channels of the polymer under bias. The thickness of the ultrathin PFN–Br interfacial layer was optimized to decrease the dark current density. An EQE of 19100% at 365 nm was obtained for DCP3-based PM-OPDs using PFN–Br as the interfacial layer under a bias of 20 V. The optimized PM-OPDs exhibit excellent stability, with no photocurrent decay after 70 days of storage in a nitrogen-filled glove box, which is attributed to the locking of donor and acceptor segments through covalent links in the polymer. The optimized PM-OPDs can be employed to measure the heart rate (HR) of humans under different pulsatile conditions, indicating the promising application prospects of PM-OPDs with a single polymer as the active layer.

Introduction

Photomultiplication-type organic photodetectors (PM-OPDs) have drawn increasing attention due to their external quantum efficiency (EQE) values of much higher than 100% and their small dark current density (J_D) values.[1–4] The small J_D values of PM-OPDs originate from the single-charge-carrier transport channels in the active layers with donor:acceptor weight ratios of $\sim$ 100 : 1 or 1 : 100, in which the presence of much less donor or acceptor will form large amounts of isolated charge traps in the bulk heterojunction active layers.[5–8] The presence of more trapped charge near the electrode will generate a Coulomb force, inducing interfacial band-bending for opposite-charge tunneling injection from the external circuit and leading to the large photocurrent density (J_L) values of PM-OPDs.[9–12] Great achievements in the field of PM-OPDs have been obtained *via* controlling molecular arrangements, charge mobility, and photogenerated exciton distributions, and *via* interfacial engineering, introducing third components, and employing double-layer strategies.[7,9,13–15] Yang and co-workers employed the liquid–crystal material BTR as a regulator to enhance the performance of PM-OPDs; thanks to the optimized molecular arrangement improving hole mobility in the active layer, the EQE value of PM-OPDs could be increased 2.5-fold upon incorporating an appropriate amount of BTR into the active layer.[15] The EQE of optimal PM-OPDs can be improved to 19300% at 660 nm under a bias of −20 V. Wu *et al.* utilized ITO/PEIE with a work function of 3.6 eV as an electrode to increase the interfacial hole injection barrier, achieving a J_D value of 2.53 × 10^{-4} mA cm^{-2} and responsivity (R) of 42.0 A W^{-1} for PM-OPDs with P3HT : $PC_{61}BM$ (100 : 1, wt/wt) as the active layer under a bias of −20 V.[14] Zhao *et al.* reported narrowband double-layered PM-OPDs with one response peak at 660 nm, a full-width at half-maximum (FWHM) of less than 35 nm, and an optimal EQE of 1120% under a bias of −20 V, in which the double-layered PM-OPDs were constructed with P3HT : P-TPD (9 : 2, wt/wt) as the optical field adjusting (OFA)

[a] Key Laboratory of Luminescence and Optical Information, Ministry of Education, Beijing Jiaotong University, Beijing, 100044, People's Republic of China. E-mail: fjzhang@bjtu.edu.cn
[b] Beijing Advanced Innovation Center for Soft Matter Science and Engineering & State Key Laboratory of Organic–Inorganic Composites, Beijing University of Chemical Technology, Beijing, 100029, People's Republic of China. E-mail: liweiwei@iccas.ac.cn
[c] Institute for Display and Sensor Devices, BOE Technology Group Co. Ltd., No. 9 Dize Road, BDA, Beijing 100176, People's Republic of China. E-mail: yuanguangcai@boe.com.cn
[d] Organic Optoelectronic Materials Laboratory, Department of Chemistry, College of Science, Korea University, 02841, Seoul, Republic of Korea

† Electronic supplementary information (ESI) available. See DOI: https://doi.org/10.1039/d2tc01297a

‡ Zijin Zhao and Baiqiao Liu contributed equally to this work.

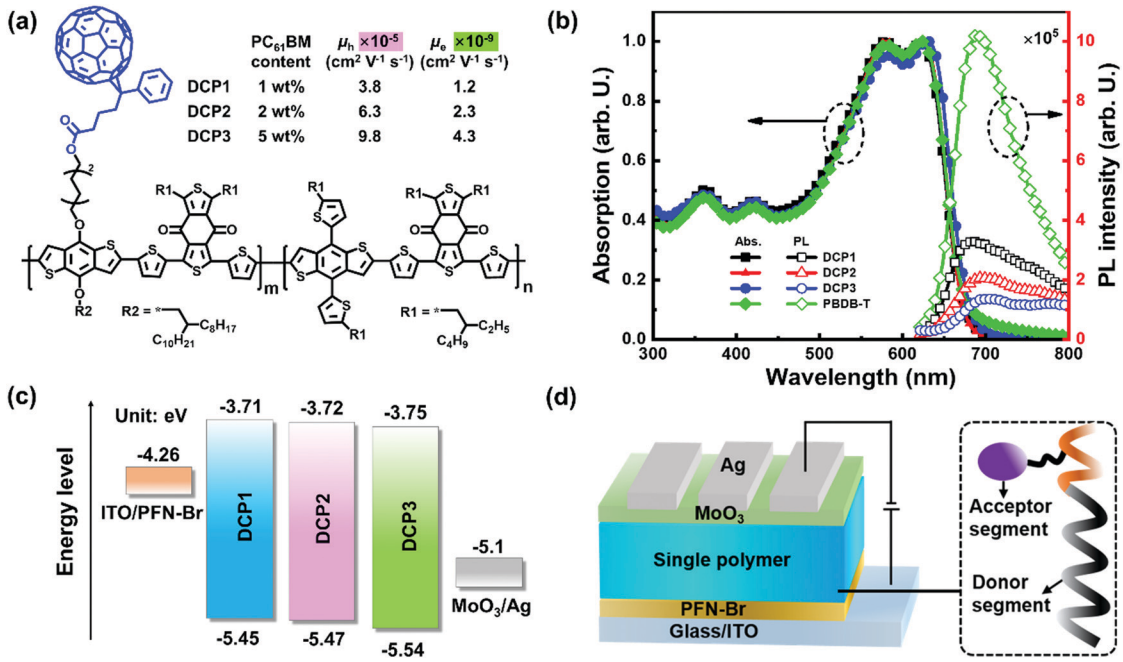

Fig. 1 (a) The chemical structures of the polymers. (b) Absorption and PL spectra of PBDB-T and polymer films. (c) Energy levels of the polymers, ITO/PFN–Br,[23] and the MoO_3/Ag electrode. (d) The device architecture of a PM-OPD with a single polymer as the active layer.

layer and P3HT : $PC_{71}BM$ (50 : 1, wt/wt) as the photomultiplication (PM) layer *via* transfer-printing technology.[16] The phase separation of two-component donor:acceptor films is usually unstable due to inevitable molecular aggregation, and this is harmful to the long-term stability of PM-OPDs.[17–19] Stability is one key prerequisite for the real-world application of PM-OPDs. However, it is highly challenging to maintain long-term stability in relation to phase separation in bulk heterojunction (BHJ) active layers.

In this work, we proposed a smart strategy to overcome the long-term stability issues connected with PM-OPDs *via* developing polymers with donor and acceptor segments locked through covalent links, in which suspended $PC_{61}BM$ in the polymers was used as an intramolecular electron trap to induce interfacial band-bending for efficient hole tunneling injection. Three fullerene-containing polymers, named DCP1-3, were synthesized according to the synthetic procedure shown in Scheme S1 (ESI†), and the chemical structures of these polymers are depicted in Fig. 1a. The molecular structures of the monomers and polymers were confirmed through ^1H and ^{13}C nuclear magnetic resonance spectra and mass spectrometry measurements, as shown in Fig. S1–S4 (ESI†). The polymers contain PBDB-T units as a conjugated backbone and donor segments. Functionalized units with $PC_{61}BM$ pendants are connected to the PBDB-T conjugated backbone through covalent links, and the attached $PC_{61}BM$ pendants are used as intramolecular electron traps. The amounts of $PC_{61}BM$ pendants in the polymers DCP1-3 are estimated to be 1 wt%, 2 wt%, and 5 wt%, respectively. The charge mobility of the polymers was measured based on the space charge limited current (SCLC) method,[20–22] as exhibited in Fig. S5 (ESI†). The hole mobility (μ_h) and electron mobility (μ_e) values of DCP1-3 are 3.8×10^{-5} and 1.2×10^{-9} $cm^2\ V^{-1}\ s^{-1}$; 6.3×10^{-5} and 4.3×10^{-9} $cm^2\ V^{-1}\ s^{-1}$; and 9.8×10^{-5} and 4.3×10^{-9} $cm^2\ V^{-1}\ s^{-1}$, respectively. The rather low μ_e values of the polymers are mainly due to the lack of successive electron transport channels in the polymers with low amounts of $PC_{61}BM$ pendants. The absorption spectra and photoluminescence (PL) spectra of the polymers DCP1-3 and PBDB-T were recorded and are shown in Fig. 1b. The absorption spectra of the polymers are almost identical with PBDB-T because the polymers are mainly constructed from PBDB-T units with only small amounts of $PC_{61}BM$ segments. It is interesting that the PL emission of the polymers is markedly quenched as the acceptor segment content increases, indicating that photogenerated excitons can be sufficiently dissociated into free charge carriers assisted by the suspended $PC_{61}BM$ segments in the polymers. The highest occupied molecular orbital (HOMO) and lowest unoccupied molecular orbital (LUMO) levels of the polymers were measured *via* the cyclic voltammetry (CV) method, as shown in Fig. S6 (ESI†). The energy levels of the used materials are illustrated in Fig. 1c; slight variations in energy levels are induced upon the incorporation of different amounts of acceptor segments. Fig. 1d displays the structure of a PM-OPD with an inverted architecture of ITO/PFN–Br/active layer/MoO_3/Ag, in which the thickness of PFN–Br was adjusted to suppress J_D and further optimize the PM-OPD performance. The optimized PM-OPDs show an EQE of 19100% at 365 nm under a bias of 20 V and they also exhibit excellent stability, with less than 2% photocurrent decay after 70 days of storage.

Results and discussion

The current density *versus* voltage (*J–V*) curves of PM-OPDs with DCP1-3 as the active layer were measured under dark

conditions and under white light illumination with an intensity of $\sim$1 mW cm^{-2}, as shown in Fig. 2a. The J_D and J_L values of PM-OPDs are enhanced with an increase in forward bias (the ITO electrode is positively biased), which is mainly attributed to enhanced hole injection and transport in response to a large electric field. The J_D and J_L values of PM-OPDs with DCP3 as the active layer are larger than those of PM-OPDs with DCP1 or DCP2 as the active layer under the same bias; this can be easily explained based on the relatively high μ_h of DCP3 (9.8×10^{-5} cm^2 V^{-1} s^{-1}). Meanwhile, the electron current passing through the PM-OPDs should be negligible due to the low μ_e of $\sim 10^{-9}$ cm^2 V^{-1} s^{-1} (compared with the μ_h value of $\sim 10^{-5}$ cm^2 V^{-1} s^{-1}) and the electron injection barrier of $\sim$1.4 eV between MoO_3/Ag and the LUMO of the polymer. Under forward bias, holes will be injected from PFN–Br/ITO into the HOMO of the polymer and transported along the channels formed by the polymers. The J_L values of all PM-OPDs are two orders of magnitude larger than the corresponding J_D values under the same forward bias, which should arise due to enhanced hole tunneling injection from PFN–Br/ITO assisted by trapped electrons in $PC_{61}BM$ pendants under light illumination. Schematic diagrams are provided to exhibit the charge dynamics in PM-OPDs under dark and light conditions, as shown in Fig. 2b. Under dark conditions, it is difficult for holes to be injected into the active layer due to the large triangular barrier separating PFN–Br/ITO electrons from the polymer HOMO, resulting in the low J_D values of the PM-OPDs.[24–26] Under illuminated conditions, photogenerated excitons can be dissociated into free charge carriers in the polymer containing $PC_{61}BM$ pendants. Photogenerated holes will be transported along the channels of the polymer and collected by the MoO_3/Ag electrode. Photogenerated electrons will be trapped by $PC_{61}BM$ pendants due to its low content in the polymer. Trapped electrons near PFN–Br/ITO will cause interfacial band-bending, narrowing the hole injection barrier from a triangular shape to a wedge shape. Holes will be readily injected into the active layer *via* tunneling through the wedge barrier, leading to large J_L values in PM-OPDs with a single polymer as the active layer. The photoinduced current density (J_{Pi}) is obtained based on the difference between J_L and J_D, representing the photo-response abilities of a PM-OPD.[27] The J_L value of a PBDB-T-based device is slightly larger than J_D, indicating the poor photo-response abilities of the PBDB-T-based device, as depicted in Fig. S7a (ESI†). The maximum EQE of the PBDB-T-based device is lower than 50% under an applied bias of 10 V without photocurrent multiplication, as shown in Fig. S7b (ESI†), indicating that the $PC_{61}BM$ pendants play a vital role in PM-OPDs with DCP1-3 as the active layer.

The EQE spectra of all PM-OPDs were obtained under a bias of 10 V, as displayed in Fig. 2c. It is apparent that all single-polymer-based PM-OPDs exhibit a broad response range from 300 to 700 nm, corresponding well with the photon harvesting range of the polymers. It is notable that DCP3-based PM-OPDs have relatively large EQEs compared to DCP1- and DCP2-based PM-OPDs under the same bias, which can be explained based on the relatively high exciton dissociation efficiency and μ_h value shown by the DCP3-based active layer. Photogenerated excitons can be sufficiently dissociated into free charges in

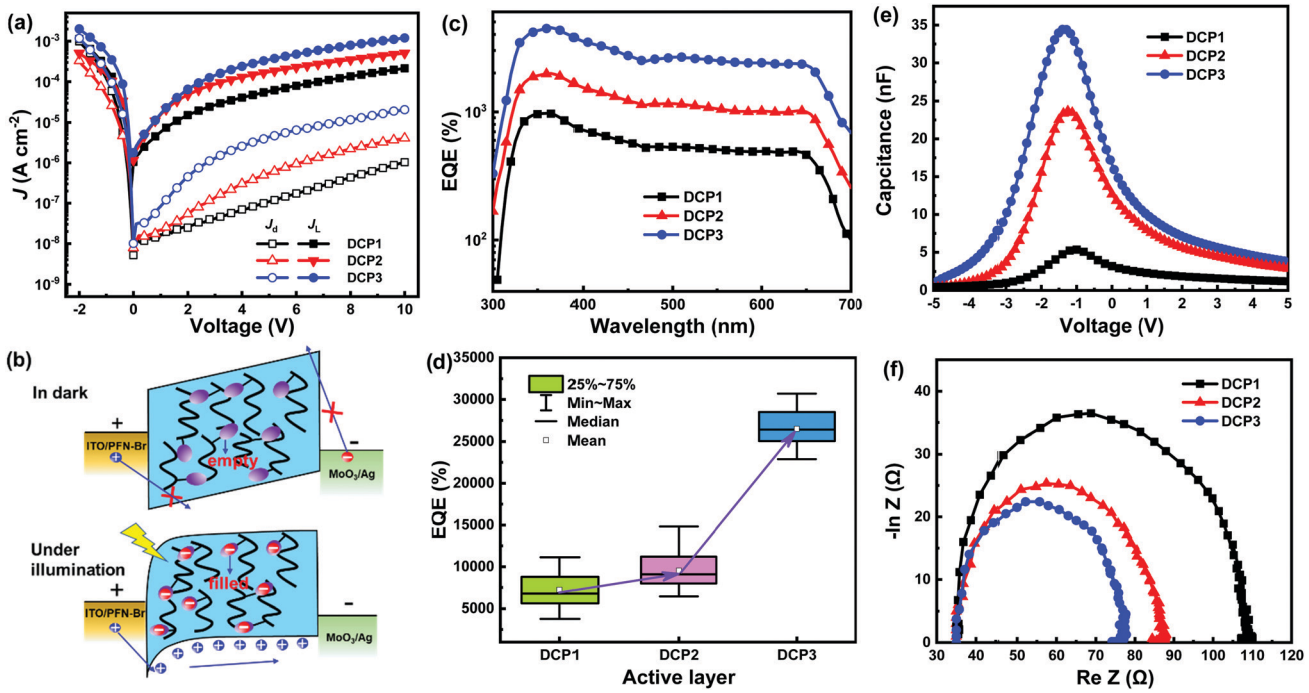

Fig. 2 (a) J–V curves of all PM-OPDs under dark and light-illumination conditions. (b) Schematic diagrams of the working mechanism of the PM-OPD. (c) The EQE spectra of all PM-OPDs under a bias of 10 V. (d) EQE box plots of all PM-OPDs; Max: maximum, Min: minimum. (e) C–V curves and (f) Nyquist plots of all PM-OPDs.

DCP3 with a relatively high $PC_{61}BM$ content, as confirmed based on the markedly quenched PL emission of DCP3 exhibited in Fig. 1b.

More photogenerated electrons will be trapped in DCP3 due to its relatively high $PC_{61}BM$ content, which can induce sufficient interfacial band-bending for hole tunneling injection. The injected holes will be sufficiently transported along the channels formed by DCP3 due to its large μ_h value of 9.8×10^{-5} cm^2 V^{-1} s^{-1} compared with those of DCP1 and DCP2. The EQE spectra of single-polymer-based PM-OPDs were measured under different biases, and these are shown in Fig. S8 (ESI†). The EQE values of all PM-OPDs rapidly increase as the bias increases, which is mainly attributed to improved hole tunneling injection and hole transport under a large bias.[28] Fig. 2d exhibits the distributions of the EQE values of all PM-OPDs under a bias of 20 V; the statistical results for each kind of single-polymer-based PM-OPD were obtained based on 15 devices prepared from different batches. The median values of the EQE distributions for DCP1-3-based PM-OPDs are 6700%, 8900%, and 26300%, respectively, under a bias of 20 V.

To investigate the charge dynamics in detail in single-polymer-based PM-OPDs, capacitance *versus* voltage (*C*–*V*) measurements were performed under one sun simulated light illumination at a frequency of 10 kHz, as exhibited in Fig. 2e. It is apparent that the capacitance of the PM-OPDs increases as the amount of $PC_{61}BM$ pendants increases in the polymers, indicating the improved electron accumulation properties of polymer films with more $PC_{61}BM$. These improved electron accumulation properties are conducive to inducing interfacial band-bending, allowing hole tunneling injection from the external circuit. The hole-transport properties of all PM-OPDs can also be investigated based on electrochemical impedance spectroscopy (EIS) measurements. Nyquist plots of all PM-OPDs were obtained in the frequency range of 10 KHz to 8 MHz under a bias of 5 V and one sun simulated light illumination, as shown in Fig. 2f. The charge transport resistance (R_{ct}) can be estimated based on the diameter of the semicircle. It is apparent that R_{ct} gradually decreases for PM-OPDs with different active layers in the order DCP1 > DCP2 > DCP3, indicating that the hole transport properties can be enhanced when using DCP3 film. The enhanced hole transport properties of DCP3 films can be attributed to the improved molecular arrangement upon incorporating more $PC_{61}BM$ pendants.

Grazing incidence wide-angle X-ray scattering (GIWAXS) analysis was carried out on polymers containing different amounts of $PC_{61}BM$ to investigate the molecular arrangements in the DCP1-3 films. The two-dimensional (2D) GIWAXS patterns of DCP1-3 films are exhibited in Fig. 3a–c, respectively. The in-plane (IP) and out-of-plane (OOP) line profiles of the GIWAXS patterns of the polymers are shown in Fig. 3d. Distinct (100) lamellar peaks ($q \approx 0.29$ Å^{-1}) and (200) lamellar peaks ($q \approx 0.65$ Å^{-1}) in the IP direction and (010) π–π stacking peaks ($q \approx 1.67$ Å^{-1}) in the OOP direction can be simultaneously observed from the profiles of the polymer films, indicating that the polymers prefer to adopt a face-on molecular orientation, allowing efficient hole transport along the normal direction to

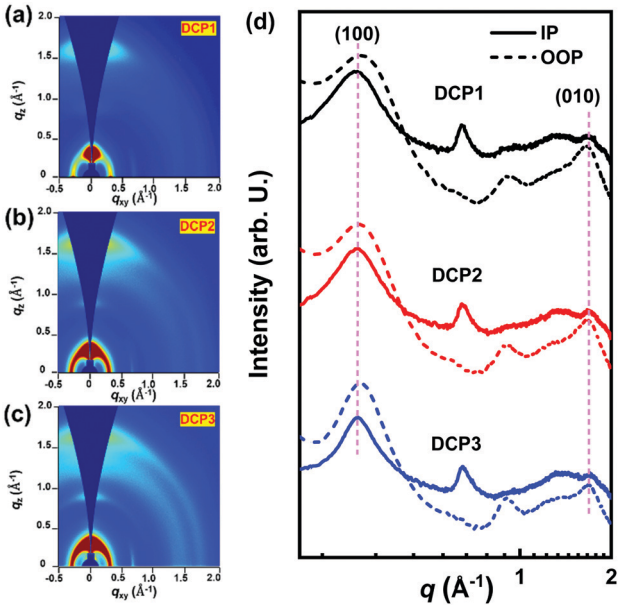

Fig. 3 (a)–(c) 2D GIWAXS patterns of DCP1-3 film samples, respectively. (d) Scattering profiles of the corresponding film samples with respect to the OOP and IP directions.

the substrate.[29,30] Meanwhile, the gradual sharpening of the IP (100) lamellar peak and OOP (010) π–π stacking peak can be clearly observed with an increase in the $PC_{61}BM$ content from the profiles of the DCP1-3 films. To evaluate the degree of molecular crystallinity, the crystal coherence length (CCL) values of the IP (100) lamellar peak and OOP (010) π–π stacking peak were calculated according to the Scherrer equation: $CCL = 2\pi k/\Delta q$,[31–33] where k denotes the Scherrer constant (≈ 0.9) and Δq denotes the FWHM of the diffraction peak. The CCL values of the IP (100) lamellar peak and OOP (010) π–π stacking peak are 6.5 nm/1.8 nm for DCP1, 7.2 nm/3.2 nm for DCP2, and 8.8 nm/3.9 nm for DCP3, respectively. The gradual increase in CCL values suggests the presence of improved molecular packing upon incorporating more $PC_{61}BM$ pendants, leading to the gradual enhancement of the μ_h value with $PC_{61}BM$ content for the polymers DCP1-3.

Specific detectivity (D^*) is a critical figure of merit for photodetectors, denoting the capacity of a photodetector to sense a faint light signal.[34–36] Supposing that shot noise mainly contributes to the total noise, D^* can be evaluated from the shot-noise-limited specific detectivity (D^*_{sh}), which can be calculated from the following equation:[37–39]

$$D^*_{sh} = \frac{R\sqrt{AB}}{i_{sh}} = \frac{R}{\sqrt{2qJ_D}}(\text{Jones}) \quad (1)$$

where R is the responsivity of the photodetector, A is the active area of the device, B is the bandwidth, i_{sh} is the shot noise current, and q is the elementary charge. The R spectra of all PM-OPDs are depicted in Fig. S9 (ESI†). The D^*_{sh} values of PM-OPDs can be obtained according to eqn (1), as shown in Fig. 4a. It is apparent that a D^*_{sh} value of over 9×10^{11} Jones can be obtained in the region of 310–700 nm for all PM-OPDs under a bias of

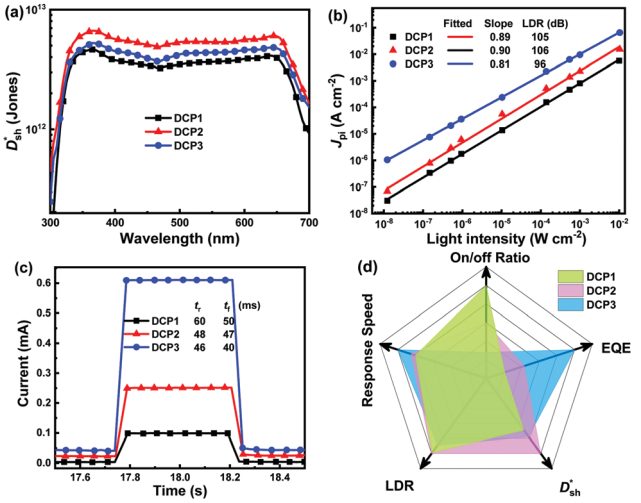

Fig. 4 Single-polymer DCP1-, DCP2-, and DCP3-based PM-OPDs: (a) D^*_{sh} spectra, (b) LDR analysis, (c) transient photocurrents of PM-OPDs under a bias of 10 V, and (d) radar map analysis of the key parameters.

10 V. The maximum D^*_{sh} values of PM-OPDs with DCP1-3 as the active layer are 4.6×10^{12}, 6.6×10^{12}, and 5.2×10^{12} Jones, respectively, under a bias of 10 V. The D^*_{sh} value of the DCP3-based PM-OPDs is lower than that of the DCP2-based PM-OPDs under a bias of 10 V owing to the relatively large J_D value of DCP3-based PM-OPDs, indicating that suppressing J_D is beneficial for enhancing the detectivity of PM-OPDs.[40,41] The linear dynamic range (LDR) describes the range over which the output signal of a photodetector changes linearly with the input signal, and this can be calculated through the equation:[42,43]

$$\mathrm{LDR} = 20 \log \frac{J_{\mathrm{upper}}}{J_{\mathrm{lower}}} (\mathrm{dB}) \quad (2)$$

where J_{upper} and J_{lower} are the maximum and minimum detectable J_{Pi} values within a linear range. The dependence of J_{Pi} on light intensity under 532 nm irradiation is depicted in Fig. 4b, with LDR values of 105, 106, and 95 dB for DCP1-3, respectively. Meanwhile, the slope of the J_{Pi}–light intensity curve of PM-OPDs with DCP3 as the active layer is 0.81, which is smaller than the value of 0.89 and 0.90 for PM-OPDs with DCP1 and DCP2, respectively, as active layers. The slope of the J_{Pi}–light intensity curve is related to charge recombination in the active layer. The relatively smaller slope of the J_{Pi}–light intensity curve of DCP3-based PM-OPDs could result from higher levels of recombination as a consequence of the higher $PC_{61}BM$ content in DCP3.

Response speed is also one of the important parameters for evaluating photodetectors.[44,45] To evaluate the response speeds of all PM-OPDs, the transient photocurrent was recorded under a bias of 10 V and 532 nm light illumination with an intensity of 10 mW cm^{-2}, and the excited light was modulated through an electronic shutter with a period of 1 s, as shown in Fig. 4c. The rise time (t_r) and fall time (t_f) decrease from 60 to 48 to 46 ms and from 50 to 47 to 40 ms, respectively, for the PM-OPDs with DCP1, DCP2, and DCP3, respectively, as the active layer. It is well known that more electron traps formed from $PC_{61}BM$ pendants can rapidly capture more photogenerated electrons, leading to sufficient interfacial band-bending as soon as possible.[46] The decreased t_r value of PM-OPDs with DCP3 as the active layer should be attributed to enhanced hole tunneling injection and better hole transport in the DCP3 film. The t_f value of the PM-OPDs corresponds to the release or recombination time of trapped electrons in $PC_{61}BM$, which strongly depends on the number of injected holes per unit time from the external circuit. Once the excited light is turned off, the injected holes will rapidly recombine with trapped electrons in $PC_{61}BM$, resulting in the termination of interfacial band-bending and limited hole tunneling injection. The shorter t_f value of PM-OPDs with DCP3 as the active layer can be well explained based on the relatively large transient photocurrent. Curves plotting the on/off current ratios of PM-OPDs were obtained according to the J–V curves of PM-OPDs in the dark and under light illumination, as exhibited in Fig. S10 (ESI†). To intuitively evaluate the overall performances of the PM-OPDs, the EQE, D^*_{sh}, LDR, response speed, and on/off ratio values of all PM-OPDs under a bias of 10 V were gathered in the form of a radar map, as illustrated in Fig. 4d. Although DCP3-based PM-OPDs exhibit the optimal EQE value and response speed, the corresponding D^*_{sh}, LDR, and on–off ratio are lower than those of the other kinds of PM-OPDs due to the relatively large J_D value of PM-OPDs with DCP3 as the active layer. To suppress the J_D value of PM-OPDs with DCP3 as the active layer, the thickness of the interfacial PFN–Br layer was finely optimized *via* adjusting the concentration of PFN–Br solution (C_{PFN-Br}) while maintaining the other preparation conditions. The thickness of the PFN–Br layer should increase along with an increase in C_{PFN-Br}.

The J–V curves of DCP3-based PM-OPDs with different PFN–Br layer thicknesses were obtained and are shown in Fig. 5a. Obviously, the J_D value of PM-OPDs is gradually reduced upon increasing C_{PFN-Br}. The hole injection barrier will be enlarged upon increasing the thickness of the PFN–Br interlayer *via* using a higher-concentration solution. It will be more difficult for holes to be injected into the active layer with increased PFN–Br layer thickness, resulting in the suppression of J_D. EIS measurements of DCP3-based PM-OPDs with different C_{PFN-Br} values under dark conditions were performed, and the results are shown in Fig. S11 (ESI†). R_{ct} clearly increases as C_{PFN-Br} is increased from 0.2 to 0.7 mg ml^{-1}, which should result from an enhanced hole injection barrier as a result of an increase in C_{PFN-Br}. The J_L value of the PM-OPDs can be kept almost constant as C_{PFN-Br} increases from 0.2 to 0.5 mg ml^{-1} but it slightly decreases as C_{PFN-Br} increases to 0.7 mg ml^{-1}. The on/off ratio of PM-OPDs can be enhanced from 58 to 397 as C_{PFN-Br} increases from 0.2 to 0.7 mg ml^{-1}, resulting from a gradual decrease in J_D, as shown in Fig. S12 (ESI†). The EQE and D^*_{sh} spectra of DCP3-based PM-OPDs with different levels of C_{PFN-Br} were investigated under a bias of 10 V, and the results are displayed in Fig. 5b and c, respectively. The EQE values of DCP3-based PM-OPDs slightly decrease as C_{PFN-Br} increases from 0.2 to 0.7 mg ml^{-1} due to the increased hole injection barrier. The maximum EQE values of DCP3-based PM-OPDs are 4510%, 4500%, 3970%, and 3040%

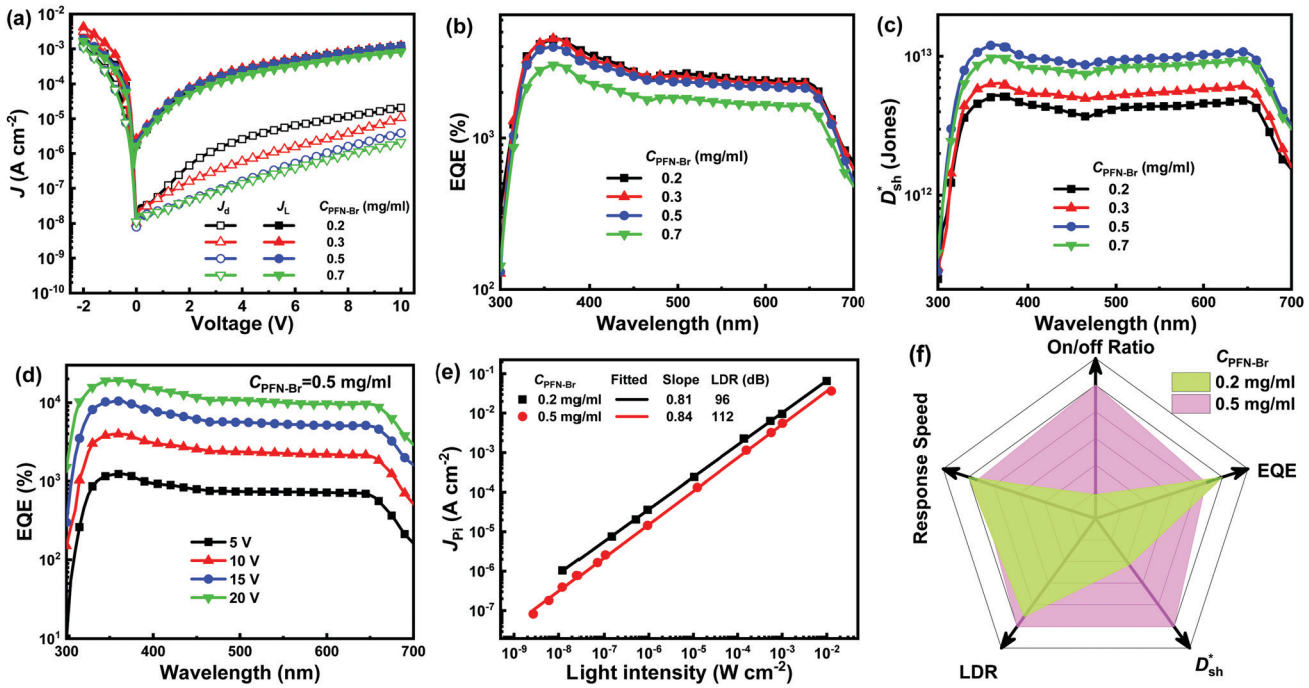

Fig. 5 (a) The J–V curves, (b) EQE spectra, and (c) D^*_{sh} spectra of DCP3-based PM-OPDs with PFN–Br layers prepared from solutions with different concentrations. (d) The EQE spectra of optimized PM-OPDs under different levels of applied bias. (e) The LDR of DCP3-based PM-OPDs with PFN–Br layers prepared from solutions with concentrations of 0.2 and 0.5 mg ml^{-1}. (f) Radar map analysis of DCP3-based PM-OPDs with PFN–Br layers prepared from solutions with concentrations of 0.2 and 0.5 mg ml^{-1}.

under a bias of 10 V when C_{PFN-Br} is 0.2, 0.3, 0.5, and 0.7 mg ml^{-1}, respectively. The D^*_{sh} values of PM-OPDs are enhanced as C_{PFN-Br} increases from 0.2 to 0.5 mg ml^{-1} thanks to the suppression of J_D, and then there is a slight decrease when C_{PFN-Br} increases to 0.7 mg ml^{-1} due to the weakened hole tunneling injection. The maximum D^*_{sh} value of 1.2×10^{13} Jones at 365 nm under a bias of 10 V can be obtained for PM-OPDs with a PFN–Br layer prepared from 0.5 mg ml^{-1} solution. The use of the optimal PFN–Br layer will lead to acceptable EQE values and rather low J_D values in PM-OPDs.

The EQE spectra of DCP3-based PM-OPDs with a PFN–Br layer prepared at a solution concentration of 0.5 mg ml^{-1} were investigated under different bias levels, and they are shown in Fig. 5d. It is apparent that the EQE values of the optimal PM-OPDs are dramatically enhanced upon increasing the bias due to enhanced hole tunneling injection from the PFN–Br/ITO electrode and accelerated hole transport in the active layer under a large electric field. An EQE of 19100% at 365 nm is achieved for the optimal PM-OPDs under a bias of 20 V. The LDR of optimal PM-OPDs was investigated *via* measuring J–V curves at different light intensities, and J_{Pi} as a function of the light intensity under a bias of 10 V is shown in Fig. 5e. The J_{Pi} values of the optimal PM-OPDs linearly vary from 2.6×10^{-2} to 1.6×10^{-7} A cm^{-2} as the light intensity decreases from 12.6 mW cm^{-2} to 2.7 nW cm^{-2}, giving a LDR of 112 dB. The LDR of the optimal PM-OPDs is larger than that of 96 dB for control PM-OPDs prepared with a C_{PFN-Br} value of 0.2 mg ml^{-1} due to the suppression of J_D. It is apparent that the slope of a curve of J_{Pi} *versus* light-intensity for the optimum PM-OPDs is larger than that of the control PM-OPDs, resulting from the suppressed recombination of trapped electrons and injected holes. The t_r and t_f values of the optimal PM-OPDs are 46 and 49 ms, respectively, which are slightly increased in comparison with those of the control PM-OPDs, resulting from the slightly weakened hole tunneling injection, as shown in Fig. S13 (ESI†). To intuitively compare the parameters of the optimal PM-OPDs and the control PM-OPDs, radar map analysis of the key parameters of EQE, D^*_{sh}, LDR, response speed, and on/off ratio is displayed in Fig. 5f. Apparently, the overall performance of PM-OPDs can be well improved and balanced *via* optimizing the thickness of the PFN–Br layer, primarily resulting from the large suppression of J_D and the maintenance of J_L.

The optimal PM-OPDs without encapsulation were stored in a nitrogen-filled glove box to investigate their long-term stability. The photocurrent of the optimal PM-OPDs was recorded under a bias of 10 V every 4 days, as shown in Fig. 6a. It is apparent that the optimal PM-OPDs exhibit less than 2% photocurrent decay after 70 days of storage, indicating the superior long-term stability of the PM-OPDs due to the polymer locking the donor and acceptor segments *via* covalent links.[47,48] The photocurrent of PBDB-T : $PC_{61}BM$ (95 : 5, w/w) BHJ-based PM-OPDs undergoes a relatively fast decay process, as shown in Fig. 6a. BHJ-based PM-OPDs show approximately 20% photocurrent decay after 57 days of storage, resulting from molecular aggregation in the blended donor:acceptor active layer. The photocurrent *versus* illumination time curve of optimal PM-OPDs after 70 days of storage is shown in the inset of Fig. 6a, indicating the excellent stability of single-polymer-based PM-OPDs.

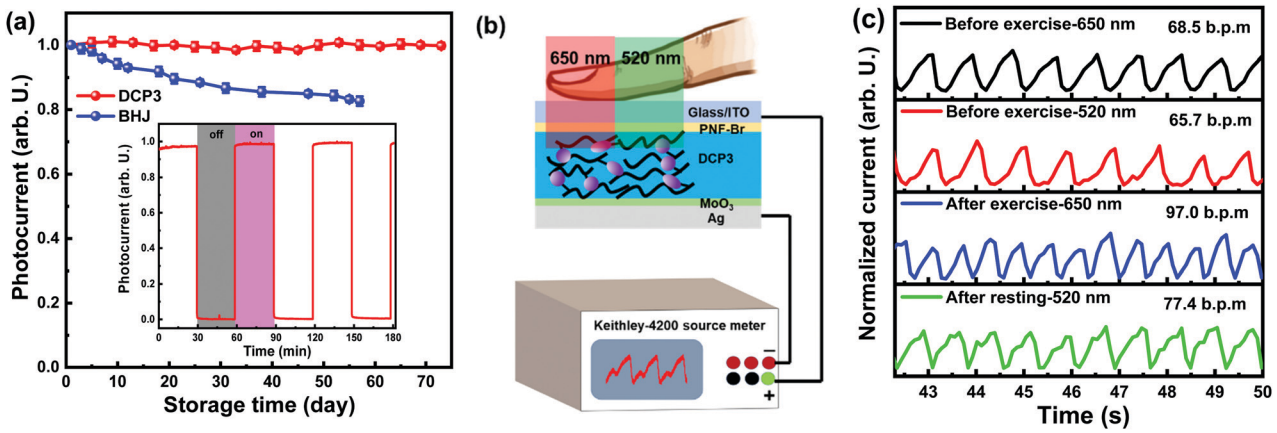

Fig. 6 (a) The normalized photocurrent of the optimal PM-OPDs and PBDB-T:$PC_{61}BM$ BHJ-based PM-OPDs under a bias of 10 V as a function of storage time. The inset shows the transient photocurrent of the optimal PM-OPDs over 3 h. (b) A diagram of the PPG measurement set-up. (c) PPG signals measured from a finger before and after exercise and after resting.

Photoplethysmography (PPG) testing was performed to demonstrate the potential application of the optimal PM-OPDs. An optimal PM-OPD was contented to a Keithley 4200 source meter to realize the application of the PPG sensor, as illustrated in Fig. 6b. When light passes through the finger, the transmitted light can be detected by the PM-OPD. The PPG signal can be obtained *via* recording the variations in photocurrent resulting from periodic variations in the transmitted light intensity due to the systolic and diastolic phases of the cardiac cycle.[49–52] The heart rate (HR) of a human can be evaluated based on the period of the PPG signal, as shown in Fig. 6c. A detailed description of the use of PM-OPDs for monitoring human heart rates is given in the ESI.† The current from the PM-OPD was monitored under a bias of 5 V in air to measure the absorption of red (650 nm) or green (520 nm) light by the blood. Clear and repeated PPG signals can be obtained using red or green light due to the high sensitivity of the optimized PM-OPDs to 650 and 520 nm light. The pulsatile signal can be distinctly extracted from the output current, and the heart rates (HRs) of one author were evaluated to be 68.5 and 65.7 beats per minute (bpm) before exercise based on red and green light, respectively. The measured HR values for the author using both red and green light are in the normal range for humans. The slight fluctuations of the HR value of the author under resting conditions should be attributed to fluctuations in the pulsatile signal. The HR value was enhanced to 97.0 bpm for the author after exercise. Then, the HR value dropped to 77.4 bpm for the author after having a rest. The PM-OPDs can be used to measure the HRs of humans under different pulsatile conditions due to the high sensitivity of PM-OPDs to slight changes in light intensity.

Conclusions

In summary, three polymers, DCP1-3, with different amounts of $PC_{61}BM$ pendants as intramolecular traps were carefully synthesized, and they were successfully applied in PM-OPDs with the configuration of ITO/PFN–Br/active layer/MoO_3/Ag. The photocurrent multiplication is attributed to hole tunneling injection from the PFN–Br/ITO electrode induced by interfacial trapped electrons in $PC_{61}BM$ pendants under forward bias. The DCP3-based PM-OPDs show the highest EQE values due to the relatively high hole-transport abilities and exciton dissociation efficiency of DCP3 film. The overall performance of DCP3-based PM-OPDs can be further enhanced *via* adjusting the thickness of the PFN–Br layer to suppress J_D. A maximum EQE of 19100% is realized under a bias of 20 V when using the optimal PM-OPDs with a PFN–Br layer prepared from solution with a concentration of 0.5 mg ml^{-1}. Meanwhile, the optimized PM-OPDs show enhanced D^*_{sh}, LDR, and on/off ratio values of 1.2×10^{13} Jones, 104 dB, and 390, respectively, under a bias of 10 V compared to values of 5.2×10^{12} Jones, 95 dB, and 58, respectively, for control PM-OPDs with a PFN–Br layer prepared from solution with a C_{PFN-Br} value of 0.2 mg ml^{-1}. PM-OPDs with a single polymer as the active layer show excellent stability after 70 days of storage without any encapsulation, indicating their great application potential. Meanwhile, the HR of an author under different pulsatile conditions can be successfully recorded, indicating the strong detection abilities of the PM-OPDs toward weak light without a current amplified circuit.

Author contributions

Z. Zhao, G. Yuan, and F. Zhang conceived the idea and wrote this paper. Z. Zhao fabricated all the PM-OPD samples, conducted measurements, and performed data analysis. B. Liu and W. Li designed and synthesized the polymers and performed the characterization. C. Xu, M. Liu, and K. Yang participated in data analysis and manuscript preparation. Z. Zhao and L. Li conducted the heart-rate measurements. S. Jeong and H. Woo conducted the GIWAXS measurements. F. Zhang directed the project.

Conflicts of interest

There are no conflicts to declare.

Acknowledgements

The authors are thankful for financial support from the Fundamental Research Funds for the Central Universities (Grant No. 2021YJS178), National Natural Science Foundation of China (Grant No. 61975006, 62175011 and 92163128), and the Beijing Natural Science Foundation (Grant No. 4192049 and JQ21006).

References

1 Z. Zhao, C. Xu, L. Niu, X. Zhang and F. Zhang, *Laser Photonics Rev.*, 2020, **14**, 2000262.
2 J. Kublitski, A. Fischer, S. Xing, L. Baisinger, E. Bittrich, D. Spoltore, J. Benduhn, K. Vandewal and K. Leo, *Nat. Commun.*, 2021, **12**, 4259.
3 M. Liu, J. Wang, Z. Zhao, K. Yang, P. Durand, F. Ceugniet, G. Ulrich, L. Niu, Y. Ma, N. Leclerc, X. Ma, L. Shen and F. Zhang, *J. Phys. Chem. Lett.*, 2021, **12**, 2937.
4 J. Kim, M. Kang, S. Lee, C. So and D. S. Chung, *Adv. Mater.*, 2021, **33**, 2104689.
5 J. Kim, C. So, M. Kang, K. M. Sim, B. Lim and D. S. Chung, *Mater. Horiz.*, 2021, **8**, 276.
6 Z. Lan, Y. Lei, W. Kin, E. Chan, S. Chen, D. Luo and F. Zhu, *Sci. Adv.*, 2020, **6**, eaaw8065.
7 J. Wang, S. C. Chen, Z. Yin and Q. Zheng, *J. Mater. Chem. C*, 2020, **8**, 14049.
8 D. K. Neethipathi, H. S. Ryu, M. S. Jang, S. Yoon, K. M. Sim, H. Y. Woo and D. S. Chung, *ACS Appl. Mater. Interfaces*, 2019, **11**, 21211.
9 Z. Zhao, J. Wang, C. Xu, K. Yang, F. Zhao, K. Wang, X. Zhang and F. Zhang, *J. Phys. Chem. Lett.*, 2020, **11**, 366.
10 H. R. Sim, M. Kang, S. H. Yu, G. H. Nam, B. Lim and D. S. Chung, *Adv. Opt. Mater.*, 2020, **9**, 2001836.
11 M. S. Jang, S. Yoon, K. M. Sim, J. Cho and D. S. Chung, *J. Phys. Chem. Lett.*, 2018, **9**, 8.
12 C. Wang, J. Lai, Q. Chen, F. Zhang and L. Chen, *Nano Lett.*, 2021, **21**, 8474.
13 S. Yoon, G. S. Lee, K. M. Sim, M. J. Kim, Y. H. Kim and D. S. Chung, *Adv. Funct. Mater.*, 2021, **31**, 2006448.
14 Y. Wu, K. Fukuda, T. Yokota and T. Someya, *Adv. Mater.*, 2019, **31**, 1903687.
15 K. Yang, Z. Zhao, M. Liu, Z. Zhou, K. Wang, X. Ma, J. Wang, Z. He and F. Zhang, *Chem. Eng. J.*, 2022, **427**, 131802.
16 Z. Zhao, M. Liu, K. Yang, C. Xu, Y. Guan, X. Ma, J. Wang and F. Zhang, *Adv. Funct. Mater.*, 2021, **31**, 2106009.
17 N. Li, J. D. Perea, T. Kassar, M. Richter, T. Heumueller, G. J. Matt, Y. Hou, N. S. Guldal, H. Chen, S. Chen, S. Langner, M. Berlinghof, T. Unruh and C. J. Brabec, *Nat. Commun.*, 2017, **8**, 14541.
18 C. Li, X. Wu, X. Sui, H. Wu, C. Wang, G. Feng, Y. Wu, F. Liu, X. Liu, Z. Tang and W. Li, *Angew. Chem., Int. Ed.*, 2019, **58**, 15532.
19 M. Jorgensen, K. Norrman, S. A. Gevorgyan, T. Tromholt, B. Andreasen and F. C. Krebs, *Adv. Mater.*, 2012, **24**, 580.
20 C. Xu, K. Jin, Z. Xiao, Z. Zhao, X. Ma, X. Wang, J. Li, W. Xu, S. Zhang, L. Ding and F. Zhang, *Adv. Funct. Mater.*, 2021, **31**, 2107934.
21 W. Xu, X. Ma, J. H. Son, S. Y. Jeong, L. Niu, C. Xu, S. Zhang, Z. Zhou, J. Gao, H. Y. Woo, J. Zhang, J. Wang and F. Zhang, *Small*, 2022, **18**, 2104215.
22 S. Zhang, X. Ma, C. Xu, W. Xu, S. Y. Jeong, H. Y. Woo, Z. Zhou, X. Zhang and F. Zhang, *Macromol. Rapid Commun.*, 2022, DOI: **10.1002/marc.202200345**.
23 L. Chen, C. Xie and Y. Chen, *Adv. Funct. Mater.*, 2014, **24**, 3986.
24 S. G. Han, H. Lee, W. Choi, D. Lee, S. Kim, Y. Sung, S. Kim and K. Cho, *Adv. Funct. Mater.*, 2021, **31**, 2102087.
25 Z. Zhao, C. Li, L. Shen, X. Zhang and F. Zhang, *Nanoscale*, 2020, **12**, 1091.
26 D. Guo, L. Yang, J. Zhao, J. Li, G. He, D. Yang, L. Wang, A. Vadim and D. Ma, *Mater. Horiz.*, 2021, **8**, 2293.
27 Z. Zhao, B. Liu, C. Xu, M. Liu, K. Yang, X. Zhang, Y. Xu, J. Zhang, W. Li and F. Zhang, *J. Mater. Chem. C*, 2021, **9**, 5349.
28 K. Yang, J. Wang, Z. Zhao, Z. Zhou, M. Liu, J. Zhang, Z. He and F. Zhang, *ACS Appl. Mater. Interfaces*, 2021, **13**, 21565.
29 L. Lv, W. Dang, X. Wu, H. Chen, T. Wang, L. Qin, Z. Wei, K. Zhang, G. Shen and H. Huang, *Macromolecules*, 2020, **53**, 10636.
30 Y. Wei, J. Yu, L. Qin, H. Chen, X. Wu, Z. Wei, X. Zhang, Z. Xiao, L. Ding, F. Gao and H. Huang, *Energy Environ. Sci.*, 2021, **14**, 2314.
31 Y. Wu, J. Guo, W. Wang, Z. Chen, Z. Chen, R. Sun, Q. Wu, T. Wang, X. Hao, H. Zhu and J. Min, *Joule*, 2021, **5**, 1800.
32 J. Kim, C. W. Joo, S. Z. Hassan, S. H. Yu, M. Kang, J. E. Pi, S. Y. Kang, Y. S. Park and D. S. Chung, *Mater. Horiz.*, 2021, **8**, 3141.
33 M. Liu, J. Wang, K. Yang, Z. Zhao, Z. Zhou, Y. Ma, L. Shen, X. Ma and F. Zhang, *J. Mater. Chem. C*, 2021, **9**, 6357.
34 Y. Yao, Q. Ou, K. Wang, H. Peng, F. Fang, Y. Shi, Y. Wang, D. I. Asperilla, Z. Shuai and P. Samori, *Nat. Commun.*, 2021, **12**, 3667.
35 C. Fuentes-Hernandez, W. Chou, T. Khan, L. Diniz, J. Lukens, F. Larrain, V. Rodriguez-Toro and B. Kippelen, *Science*, 2020, **370**, 698.
36 X. Wang, L. Lv, L. Li, Y. Chen, K. Zhang, H. Chen, H. Dong, J. Huang, G. Shen, Z. Yang and H. Huang, *Adv. Funct. Mater.*, 2016, **26**, 6306.
37 Y. Chen, Y. Zheng, Y. Jiang, H. Fan and X. Zhu, *J. Am. Chem. Soc.*, 2021, **143**, 4281.
38 Y. Wei, H. Chen, T. Liu, S. Wang, Y. Jiang, Y. Song, J. Zhang, X. Zhang, G. Lu, F. Huang, Z. Wei and H. Huang, *Adv. Funct. Mater.*, 2021, **31**, 2106326.
39 T. Yokota, K. Fukuda and T. Someya, *Adv. Mater.*, 2021, **33**, 2004416.
40 B. Park, J. Jung, D. H. Lim, H. Lee, S. Park, M. Kyeong, S. J. Ko, S. H. Eom, S. H. Lee, C. Lee and S. C. Yoon, *Adv. Funct. Mater.*, 2021, **31**, 2108026.

41 W. Jang, B. G. Kim, S. Seo, A. Shawky, M. S. Kim, K. Kim, B. Mikladal, E. I. Kauppinen, S. Maruyama, I. Jeon and D. H. Wang, *Nano Today*, 2021, **37**, 101081.
42 J. Liu, J. Jiang, S. Wang, T. Li, X. Jing, Y. Liu, Y. Wang, H. Wen, M. Yao, X. Zhan and L. Shen, *Small*, 2021, **17**, 2101316.
43 C. Li, H. Wang, F. Wang, T. Li, M. Xu, H. Wang, Z. Wang, X. Zhan, W. Hu and L. Shen, *Light: Sci. Appl.*, 2020, **9**, 31.
44 A. Pospischil, M. Humer, M. M. Furchi, D. Bachmann, R. Guider, T. Fromherz and T. Mueller, *Nat. Photonics*, 2013, **7**, 892.
45 J. Vanderspikken, W. Maes and K. Vandewal, *Adv. Funct. Mater.*, 2021, **31**, 2104060.
46 Z. Zhao, B. Liu, C. Xie, Y. Ma, J. Wang, M. Liu, K. Yang, Y. Xu, J. Zhang, W. Li, L. Shen and F. Zhang, *Sci. China: Chem.*, 2021, **64**, 1302.
47 Y. He, T. Heumüller, W. Lai, G. Feng, A. Classen, X. Du, C. Liu, W. Li, N. Li and C. J. Brabec, *Adv. Energy Mater.*, 2019, **9**, 1900409.
48 S. Liang, X. Jiang, C. Xiao, C. Li, Q. Chen and W. Li, *Acc. Chem. Res.*, 2021, **54**, 2227.
49 Y. Khan, A. E. Ostfeld, C. M. Lochner, A. Pierre and A. C. Arias, *Adv. Mater.*, 2016, **28**, 4373.
50 S. Park, K. Fukuda, M. Wang, C. Lee, T. Yokota, H. Jin, H. Jinno, H. Kimura, P. Zalar, N. Matsuhisa, S. Umezu, G. C. Bazan and T. Someya, *Adv. Mater.*, 2018, **30**, 1802359.
51 J. Liu, Y. Wang, H. Wen, Q. Bao, L. Shen and L. Ding, *Sol. RRL*, 2020, **4**, 2000139.
52 G. Simone, D. Tordera, E. Delvitto, B. Peeters, A. J. J. M. Breemen, S. C. J. Meskers, R. A. J. Janssen and G. H. Gelinck, *Adv. Opt. Mater.*, 2020, **8**, 1901989.

